

PHOTONICS Research

Polarization-insensitive interferometer based on a hybrid integrated planar light-wave circuit

GUO-WEI ZHANG,^{1,2} YU-YANG DING,^{3,6} WEI CHEN,^{1,2,7}  FANG-XIANG WANG,^{1,2}  PENG YE,^{1,2}
GUAN-ZHONG HUANG,^{1,2} SHUANG WANG,^{1,2}  ZHEN-QIANG YIN,^{1,2} JUN-MING AN,^{4,5}
GUANG-CAN GUO,^{1,2} AND ZHENG-FU HAN^{1,2}

¹CAS Key Laboratory of Quantum Information, University of Science and Technology of China, Hefei 230026, China

²CAS Center for Excellence in Quantum Information and Quantum Physics, University of Science and Technology of China, Hefei 230026, China

³Hefei Guizhen Chip Technologies Co., Ltd., Hefei 230000, China

⁴State Key Laboratory on Integrated Optoelectronics, Institute of Semiconductors, Chinese Academy of Sciences, Beijing 100083, China

⁵Center of Materials Science and Optoelectronics Engineering, University of Chinese Academy of Sciences, Beijing 100049, China

⁶e-mail: dingyuyang@gz-ichip.com

⁷e-mail: weich@ustc.edu.cn

Received 25 May 2021; revised 1 August 2021; accepted 25 August 2021; posted 26 August 2021 (Doc. ID 432327); published 6 October 2021

Interferometers are essential elements in classical and quantum optical systems. The strictly required stability when extracting the phase of photons is vulnerable to polarization variation and phase shift induced by environment disturbance. Here, we implement polarization-insensitive interferometers by combining silica planar light-wave circuit chips and Faraday rotator mirrors. Two asymmetric interferometers with temperature controllers are connected in series to evaluate the single-photon interference. Average interference visibility over 12 h is above 99%, and the variations are less than 0.5%, even with active random polarization disturbance. The experiment results verify that the hybrid chip is available for high-demand applications like quantum key distribution and entanglement measurement. © 2021 Chinese Laser Press

<https://doi.org/10.1364/PRJ.432327>

1. INTRODUCTION

Photons are the most critical information carriers and perform high-fidelity operations in up-to-date information-processing systems. The interferometer plays an essential role in various information-processing applications, either in classical or quantum research fields, including metrology and sensing [1], coherent optical communication [2], quantum entanglement measurement [3], quantum communication [4–7], and many other fields [8–12].

Interference visibility and stability are the most concerning issues when designing an interferometer. The former relates to measurement precision, and the latter decides whether the system can operate for a long time effectively. Notably, the recent advancements of the applications like quantum information processing require high-performance interferometers. For example, quantum key distribution (QKD) is one of the most promising quantum information technologies that has been deployed in the laboratory and field. For most of the phase-encoded QKD systems, the intrinsic part of the quantum bit error rate (QBER) induced by the optical components is correlated with the interference visibility V [13], of which the typical value is $(1 - V)/2$. According to the decoy-state

method [14] for practical BB84 [5] QKD systems, the secure key rate (SKR) will significantly decrease when the QBER increases. Therefore, the interferometer should have high fidelity and keep stable in these applications.

The temperature fluctuation, vibration, and stress variety in the environment will affect the birefringence of the optical components and fibers, which will disturb the polarization of the interfering photons. By monitoring the interference visibility, we can evaluate this disturbance. Since the birefringence in fiber channels is inevitable and uncontrollable, it is a more critical challenge to practical fiber QKD [15]. Many countermeasures have been proposed to overcome polarization disturbance [13,16–20], which can be classified into active and passive categories. Active polarization compensating components have been adopted in practical QKD systems [16–18], which is effective but may increase the complexity, insertion loss, and time-consumption of the system. Birefringence variations can be automatically compensated for in QKD systems using passive schemes, such as the “plug-and-play” system [19], Faraday–Michelson system [13], and Faraday–Sagnac–Michelson system [20]. Although the two-way system like plug-and-play system may suffer from Trojan horse attacks [21], these schemes have been deployed in complex field

environments and demonstrated their low QBER and outstanding long-term stability.

For applications like QKD, a pair of asymmetric interferometers is typically placed in different locations. The difference in ambient temperature of the interferometers induces a phase drift that causes the variations of visibility. Generally, we can compensate for the phase shift using phase shifters [22] or eliminate it by isolating the interferometers from complex environments. Although the influence of the temperature variations can be partially resolved using these measures, it is still an engineering challenge to keep long-term stability and high visibility of the interferometers with large arm-length differences for their high sensitivity.

The rapid development of integrated photonics points out a way to solve most of the problems mentioned above [23–25]. Some integrated QKD experiments have been reported recently [26–31], most of which use asymmetric Mach–Zehnder interferometers (AMZIs) for photon phase measurement. The integrated photonic chips (IPCs) make the system stabler in terms of temperature variations and vibrations. However, since most of the waveguides of the IPC platform are polarization-dependent, chip-based QKD systems still suffer from polarization disturbance due to varying birefringence in the channel.

Nambu *et al.* [26] and Li *et al.* [32] have studied the silica planar light-wave circuit (PLC) platform and proposed solutions to overcome this inherent challenge of dependency on polarization. The existing schemes need to control the PLC at a specific temperature with an accuracy of better than 0.05°C. The appropriate temperature working points are the birefringence of the chip, which comes from residual stress during fabrication, and is difficult to control accurately. As a result of this uncertainty, each sample should be tested separately. When the proper working points are far away from the room temperature, the energy consumption will increase. The control modules should also have a wider dynamic range and better precision control. In a complex environment, the trade-off between large dynamic range and high accuracy may decrease system performance.

We implement and evaluate a hybrid integrated design for asymmetric Faraday–Michelson interferometers (AFMIs) by combining a silica-on-silicon PLC chip and Faraday rotator mirrors (FMs). We cascade two AFMIs and evaluate their interference visibility at the single-photon level. Experimental results show that these interferometers can achieve an average interference visibility of above 99% over 12 h, and the visibility variations are less than 0.5% with an active random polarization perturbation. We verify that the polarization-independent high visibility can be obtained over a wide temperature range from 10°C to 35°C. We also propose a method to calculate the delay difference between two AFMIs using the single-photon interference results, which is essential for QKD systems.

2. DESIGN OF THE AFMI AND EXPERIMENTAL SETUPS

The scheme of the hybrid integrated AFMI is illustrated in Fig. 1(a). The PLC chip contains a directional coupler (DC) with a splitting ratio of 50:50 and two asymmetric waveguides acting as the two arms of the interferometer. Two FMs [19] are

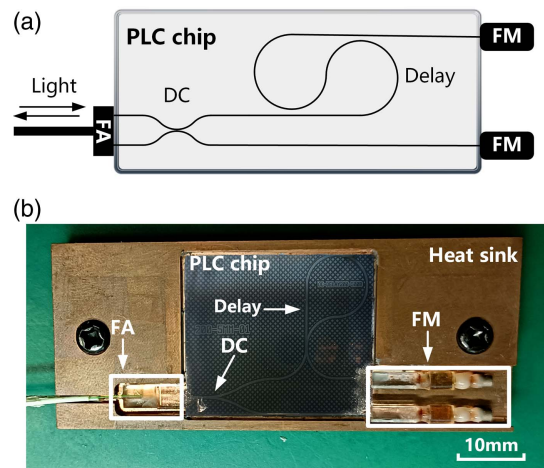


Fig. 1. AFMI device. (a) Scheme of our AFMI. The interferometer combines an FA for photon coupling, a DC with the splitting ratio of 50:50, a 200 ps delay line, and two FMs; (b) photograph of our AFMI. The size of the chip is about 27.8 mm × 23.1 mm, and the length of the FM is about 17.5 mm. A copper heat sink with a TEC and a thermistor is attached to the back of the chip. The entire system is packaged in an aluminum box with temperature isolation (not shown in this figure).

coupled and glued to the edge of two waveguides and reflect the photons back to the entrance coupled with a fiber array (FA).

The silica PLC platform is used to implement the structure, taking advantage of its relatively low transmission and coupling loss, which are essential for QKD decoders to get a higher SKR. The refractive index difference of the PLC chip for the waveguide core and cladding is 0.75%, and the geometry of the core is 6 μm × 6 μm, which is optimized to minimize the propagation loss and the coupling loss to single-mode fibers at around 1550 nm. It is worth mentioning that the chip size can be drastically reduced if we adopt the silica with a higher refractive index difference like 2.0% in the future. The fabrication flow of the PLC chip can be briefly described as follows. First, a 16 μm-thick down cladding layer is formed by thermal oxidation on a silicon substrate. A 6 μm-thick GeO₂–SiO₂ core layer is formed using plasma-enhanced chemical vapor deposition (PECVD), and then patterned using photolithography and inductively coupled plasma (ICP) etching. PECVD is employed to deposit a 20 μm thick boro-phospho-silicate glass (BPSG) upper cladding layer. Finally, the chip is annealed and packaged with two off-the-shelf Faraday mirrors to make up the AFMI structure. The optical group delay between the two arms after the DC is 200 ps, and thus the round-trip delay of the AFMI is 400 ps, which is appropriate for the phase-encoding QKD system with a pulse repetition rate of 1.25 GHz. A photograph of the hybrid integrated AFMI is shown in Fig. 1(b). A copper heat sink with a thermoelectric cooler (TEC) and a thermistor is packaged with the PLC chip as the temperature control unit, which can be used to stabilize and modulate the relative phase of the two arms of the AFMI at an accuracy of 0.01°C.

The effect of the FM is to transform an arbitrary input polarization state of the photons into its orthogonal polarization state. If we define the Jones vector of an input state as J_{in} , the function can be described as [33]

$$\text{FM} \cdot J_{\text{in}} = \text{FM} \cdot \begin{bmatrix} j_1 \\ j_2 \end{bmatrix} = \begin{bmatrix} j_2^* \\ -j_1^* \end{bmatrix} \equiv J_{\text{in}}^\perp \quad (1)$$

Suppose the Jones matrix of a waveguide is T , which is an arbitrary two-by-two matrix describing the wavelength-dependent polarization rotations and the polarization-dependent loss. The photon state behind the DC is represented as J_{in}' . The overall forward and backward transmission process through the waveguide and reflected by the FMs can be written as

$$\begin{aligned} J_{\text{out}} &= \overleftarrow{T} \cdot \text{FM} \cdot \overrightarrow{T} \cdot J_{\text{in}}' \\ &= \begin{bmatrix} A & B \\ C & D \end{bmatrix}^\dagger \cdot \text{FM} \cdot \begin{bmatrix} A & B \\ C & D \end{bmatrix} \cdot J_{\text{in}}' \\ &= \det(T^*) J_{\text{in}}'^\perp, \end{aligned} \quad (2)$$

where \rightarrow and \leftarrow mean the forward and backward propagation through the waveguide. Equation (2) shows that the polarization state of a photon backward to the DC is always orthogonal to J_{in}' with a global phase vibration regardless of the specific character of the waveguide. When the photon pulses are transferred through the long and short arms of the interferometer and then interfere at the DC, the output can be expressed as

$$I_{\text{out}} = \frac{\kappa^2}{8} [1 + \cos(\Delta\theta)] I_{\text{in}}, \quad (3)$$

where κ is the factor representing the total loss, and $\Delta\theta$ is the phase difference of the two interfering beams over the interferometers and the channel. Maximum and minimum interference intensity $I_{\text{out}}^{\text{max}}$ and $I_{\text{out}}^{\text{min}}$ can be acquired when $\Delta\theta$ is equal to 0 and π , respectively. We can calculate the interference fringe visibility using

$$V = \frac{I_{\text{out}}^{\text{max}} - I_{\text{out}}^{\text{min}}}{I_{\text{out}}^{\text{max}} + I_{\text{out}}^{\text{min}}} = \frac{\kappa^2/4 - 0}{\kappa^2/4 + 0} = 1. \quad (4)$$

This result indicates that the hybrid integrated AFMI can provide perfect interference with arbitrary input polarization states in principle, which means that the structure can compensate for the polarization perturbation in the chip and the fiber channel.

Figure 2 shows the experimental setup to evaluate the polarization independence and the stability of the hybrid integrated AFMI. We cascade two AFMIs, which act as the optical encoder and decoder module in phase-encoding QKD systems.

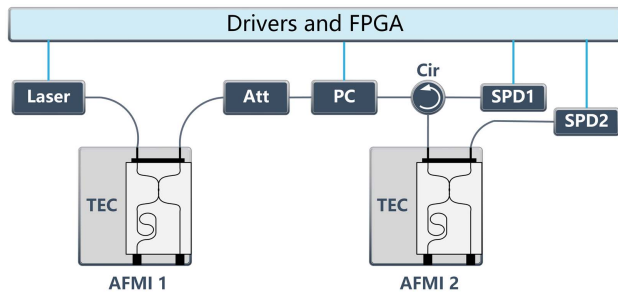


Fig. 2. Experimental setup to evaluate the characteristics of our AFMIs. Laser, gain-switch laser source; TEC, temperature controller; ATT, light attenuator; PC, polarization controller; Cir, circulator; SPD1 and SPD2, single-photon detectors.

The insertion loss of the AFMI1 and AFMI2 is 3.99 and 3.31 dB, respectively. The light source is a gain-switch semiconductor laser (Qasky WT-LD200-D) with a pulse width of 50 ps and a central wavelength at 1550 nm. A controllable attenuator and a polarization controller (PC) are placed between the two AFMIs to control the light pulses' intensity and polarization. The intensity of the light pulses is attenuated to about 0.1 photons per pulse when entering the single-photon detectors (SPDs) to simulate the single-photon interference in QKD systems. The PC is used to simulation the polarization disturbance in the long-haul fiber channel. A circulator (Cir) is placed before the AFMI2 to collect one of the two light beams after interference. Therefore, we can measure both the constructive and destructive ports of the interferometer simultaneously. We adopt two SPDs (Qasky QCRP-SPD-01) with a repetition rate of 1.25 GHz to detect the photon of the interfering peak.

The temperature variation of the chips will change the phase of the two arms and affect $\Delta\theta$ in Eq. (3). When using an SPD to monitor one port of the interferometer, I in Eq. (4) should be replaced with the counting rate C of the SPD, and V can be calculated using $V = (C_{\text{max}} - C_{\text{min}})/(C_{\text{max}} + C_{\text{min}})$, where C_{max} and C_{min} represent the maximum and minimum counting rate of the SPD (dark counts have been subtracted), respectively.

3. RESULTS

We first measure the temperature manipulation parameters of the PLC-based AFMIs without any disturbance. We maintain the temperature of one AFMI (AFMI1 in Fig. 2) at 24°C and adjust the TEC to regulate AFMI2's temperature. The normalized counting rate is shown in Fig. 3, from which we can see that the π phase modulation temperature is about 0.91°C.

To examine whether this PLC-based AFMI is immune to the polarization disturbance, we next use a PC (Keysight N7788B) to modulate the polarization state of the light input to the AFMI2. The PC can act as a polarization scrambler or set the photons to specific polarization states. We first track the states to one of the six basis states among the Stokes space [34], including linearly polarized, LP0° (1,0,0), LP45° (0,1,0), LP90° (-1,0,0), LP135° (0,-1,0), right-handed circularly polarized, RHC(0,0,1), and left-handed circularly polarized, LHC(0,0,-1). We fix the temperature of AFMI1 at 24°C and scan the AFMI2's temperature with a step of approximately 5°C. The visibility

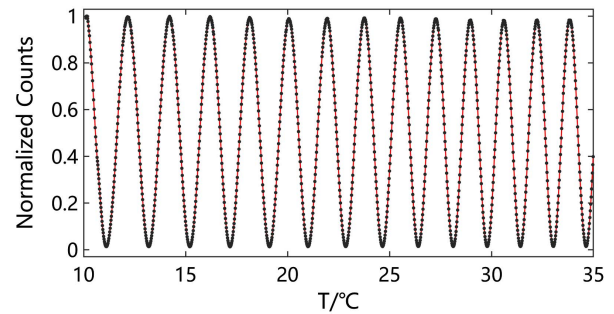


Fig. 3. Interference results with temperature scanning of AFMI1. The black dots are measured data points, and the red line is the corresponding curve fitting.

obtained at each temperature working point is shown in Fig. 4. The minimum and maximum visibilities are 98.75% and 99.25%, respectively. The slight fluctuations of the visibilities may be due to the imperfections of the FM devices.

We also evaluate the interference stability of the AFMIs with random polarization scrambling. We first adjust the interferometers to their maximum interfering point by tuning the temperature of AFMI1 and AFMI2 to 24°C and 24.66°C, respectively. Since the light intensities from the two ports are anticorrelated in principle, the counting rates of SPD1 and SPD2 should reach their maximum and minimum at the same time. We detect single-photon signals from the two ports of the interferometer simultaneously and collect the counting rate every second, which are denoted as $C_{\text{SPD1 max}}$ and $C_{\text{SPD2 min}}$, respectively. We evaluate the visibility and the variation of $\Delta\theta$ using $(C_{\text{SPD1 max}} - C_{\text{SPD2 min}})/(C_{\text{SPD1 max}} + C_{\text{SPD2 min}})$ in the following experiments.

The visibilities with and without random polarization scrambling are shown in Fig. 5(a), which are in the first and the second hour, respectively. In the first hour, the visibilities fluctuate slightly due to the practical control precision of the TEC and the counting fluctuations of the SPDs. When adding the random polarization scrambling, the average interference visibility drops slightly from 99.13% to 98.93%. The fluctuations relatively increase with the range less than 1%, which may also be due to the imperfections of FM devices.

Then we fix the temperature of AFMI1 at 24°C and modify AFMI2's temperature from 10°C to 35°C to evaluate the impact of temperature variations on the visibilities. The average value and the standard deviation (SD) of the visibility are calculated using the data collected every 10 min. The visibilities with and without polarization scrambling are shown in Fig. 5(b), in which the average fringe visibility is about $99.10\% \pm 0.04\%$ and $98.93\% \pm 0.18\%$ with fixed polarization states and random polarization scrambling, respectively.

Besides the polarization of photons, phase stability is also an essential factor affecting the interference results in practical scenarios. We initialize the temperatures of the two chips at their maximum interference working points, keep the temperature steady, and then perform a free-running measurement over 12 h. The average visibilities are calculated every 10 min, as shown in Fig. 6. It can be seen that visibilities with and without polarization scrambling are $99.14\% \pm 0.07\%$ and $98.89\% \pm 0.20\%$, respectively.

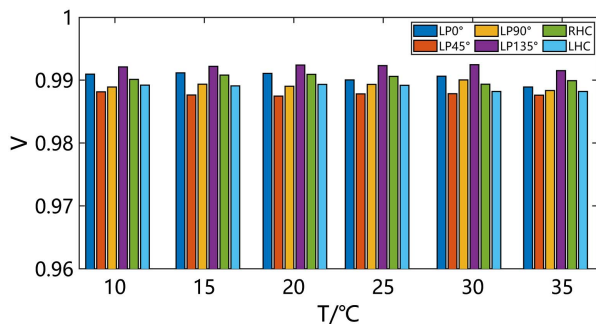


Fig. 4. Interference results for fixed polarization states.

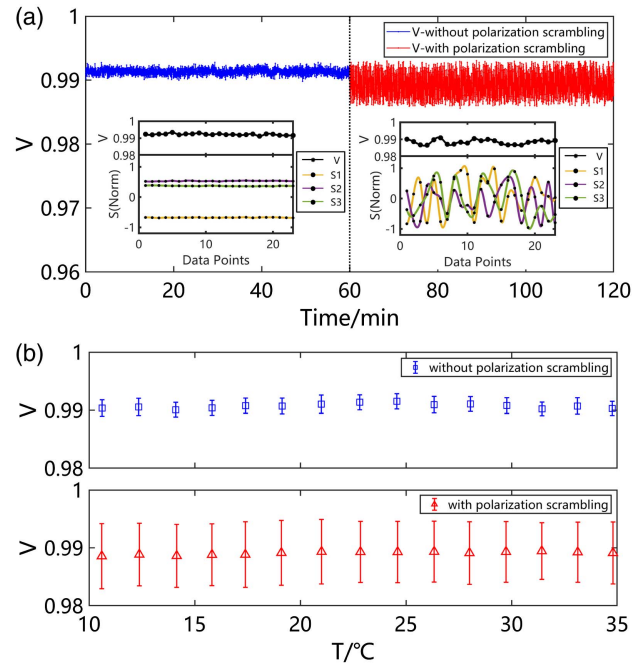


Fig. 5. Results of continuous polarization scramble test. (a) Diagram of interference visibility with and without continuous polarization scramble; insets, the diagram of normalized Stokes parameters and interference visibility during test; (b) visibilities in the range of 10°C–35°C with and without polarization scramble. The 3σ error bar is selected as the confidence interval using 10 min testing data.

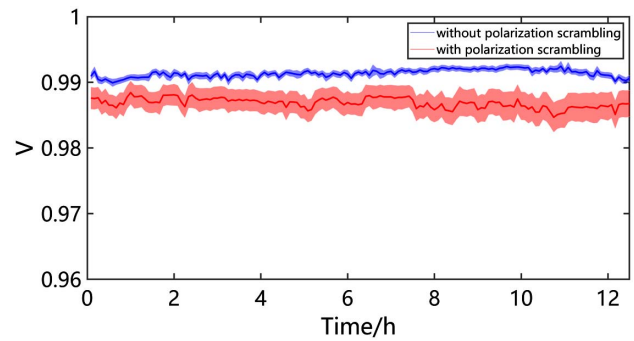


Fig. 6. Results of long-term phase stability test. Shadow areas represent the 1σ error bar.

The above results indicate that this hybrid integrated AFMI scheme can keep high and stable interference visibilities with arbitrary polarization states over a wide temperature range, which is beneficial for highly demanding applications like QKD. Furthermore, to implement high interfering visibilities between multiple interferometers is a fundamental requirement to support multiuser applications like a QKD network. How to fabricate uniform interferometers is a technical challenge. We derive the method to calculate the arm length or the optical delay difference between the two AFMIs using the interference results. We consider two pulses generated by a gain-switched distributed feedback (DFB) laser and pass through a pair of

AFMIs with 50:50 DCs, which is a typical setup in QKD systems up to date. The two pulses can be represented by [35]

$$E_k(t) = \sqrt{I_k(t - t_k)} \exp\{2\pi i[\nu_k(t - t_k) + \beta(t - t_k)^2 + \phi_k]\}, \quad (5)$$

where $k = \{1, 2\}$, and $\nu_k(t)$ is the center frequency of the wave packets that is set to 1550 nm in this article. β is the parameter accounting for frequency chirp, which is about 0.01 ps^{-2} for a typical DFB laser. ϕ_k is the phase of the light pulses. $I_k(t) = A_k \exp(-t^2/2\tau_p^2)/(\tau_p\sqrt{2\pi})$ is the temporal profile of a Gaussian laser pulse, where A_k is the total intensity of the pulses, and τ_p is the temporal width of the pulses, which is about 50 ps in our experiment. The mismatch of the time and amplitude between the two pulses is defined as $\Delta t = t_2 - t_1$ and $\Delta A = A_2/A_1$, separately. Considering the function of the beam splitter and integrating over the finite response time within the pulse width, the interference results can be written as

$$I_{\text{out}} = \frac{A_1 + A_2}{2} \pm \sqrt{A_1 A_2} \cos(\Delta\phi) \times \exp\left[-\frac{\Delta t^2}{8\tau_p^2}(1 + 16\beta^2\tau_p^4)\right], \quad (6)$$

where $\Delta\phi$ is the phase difference of the two interfering pulses, and the \pm sign represents the two output ports of the beam splitter. According to the definition of visibility, we have

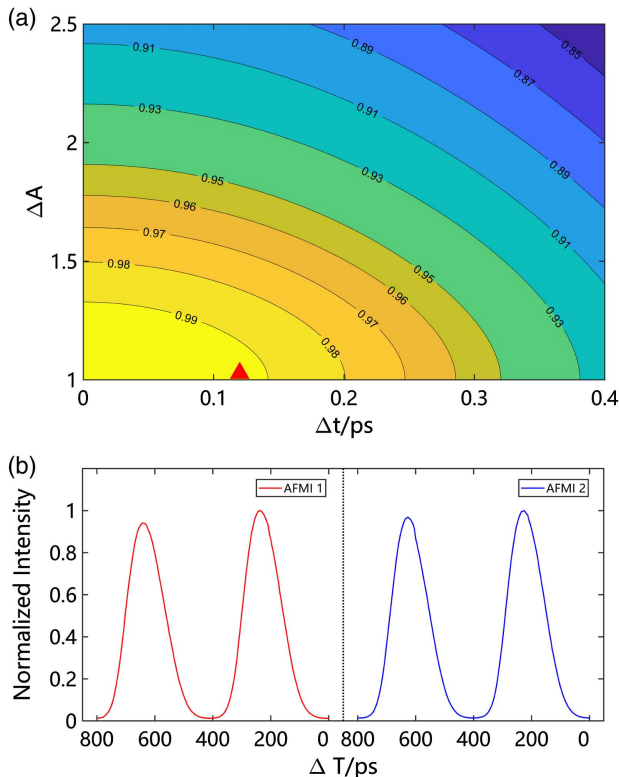


Fig. 7. Results of delay difference calculation. (a) Variations of the visibilities for temporal and amplitude mismatch. The red triangle is where our AFMIs stand. (b) Normalized light intensity after propagating through two AFMIs, detected by an SPD. The ΔT represents relative delay time.

$$V = \frac{2\sqrt{\Delta A}}{1 + \Delta A} \exp\left[-\frac{\Delta t^2}{8\tau_p^2}(1 + 16\beta^2\tau_p^4)\right]. \quad (7)$$

From Eq. (7), the visibility is affected by the mismatch of the time (Δt) and amplitude (ΔA), as shown in Fig. 7(a).

As shown in Fig. 7(b), the peak-to-peak ratio between the two peaks passing through the two AFMIs is 0.969 and 0.942, respectively. Then the corresponding ΔA is equal to 1.0287. The average visibility we obtained in the experiment is 99.25%. Therefore, we can calculate that the delay difference between the two AFMIs Δt is about 120 fs, according to Eq. (7). The mismatch can be attributed to errors in fabrication, such as the differences in coupling loss and distance between the PLC chips and FMs. However, according to this method, we can finely adjust the coupling in real time based on the single-photon detecting results and the visibility calculated.

4. CONCLUSION

In conclusion, we implement a hybrid integrated AFMI structure by combining a PLC chip with Faraday mirrors. We experimentally demonstrate that the chips have high interference visibilities and can tolerate the polarization disturbance over a wide temperature range. This characteristic makes the chips more robust to the environment and can reduce energy consumption. The delay difference of the interferometers can be precisely measured online using interference results and the model proposed in the text, which will benefit mass production and high-requirement applications in the future.

Funding. National Natural Science Foundation of China (61627820, 61622506, 61822115); National Key Research and Development Program of China (2018YFA0306400); Anhui Initiative in Quantum Information Technologies (AHY030000).

Acknowledgment. We would like to acknowledge Chang Ling Zou for useful discussions. This work was partially carried out at the USTC Center for Micro and Nanoscale Research and Fabrication, and we thank Wen Liu for helpful discussions on manufacturing and packaging.

Disclosures. The authors declare no conflicts of interest.

Data Availability. Data underlying the results presented in this paper are not publicly available at this time but may be obtained from the authors upon reasonable request.

REFERENCES

1. T. Yoshizawa, *Handbook of Optical Metrology: Principles and Applications* (CRC Press, 2017).
2. T. Okoshi and K. Kikuchi, *Coherent Optical Fiber Communications* (KTK Scientific, 1988).
3. I. Ali Khan and J. C. Howell, "Experimental demonstration of high two-photon time-energy entanglement," *Phys. Rev. A* **73**, 031801 (2006).
4. N. Gisin, G. Ribordy, W. Tittel, and H. Zbinden, "Quantum cryptography," *Rev. Mod. Phys.* **74**, 145–195 (2002).
5. C. H. Bennett and G. Brassard, "Quantum cryptography: public key distribution and coin tossing," *Theor. Comput. Sci.* **560**, 7–11 (2014).

6. H.-K. Lo, M. Curty, and K. Tamaki, "Secure quantum key distribution," *Nat. Photonics* **8**, 595–604 (2014).
7. F. Xu, X. Ma, Q. Zhang, H.-K. Lo, and J.-W. Pan, "Secure quantum key distribution with realistic devices," *Rev. Mod. Phys.* **92**, 025002 (2020).
8. D. Bouwmeester, J.-W. Pan, K. Mattle, M. Eibl, H. Weinfurter, and A. Zeilinger, "Experimental quantum teleportation," *Nature* **390**, 575–579 (1997).
9. H.-J. Briegel, W. Dür, J. I. Cirac, and P. Zoller, "Quantum repeaters: the role of imperfect local operations in quantum communication," *Phys. Rev. Lett.* **81**, 5932–5935 (1998).
10. E. Knill, R. Laflamme, and G. J. Milburn, "A scheme for efficient quantum computation with linear optics," *Nature* **409**, 46–52 (2001).
11. J. C. Adcock, C. Vigliar, R. Santagati, J. W. Silverstone, and M. G. Thompson, "Programmable four-photon graph states on a silicon chip," *Nat. Commun.* **10**, 3528 (2019).
12. S. Paesani, Y. Ding, R. Santagati, L. Chakhmakchyan, C. Vigliar, K. Rottwitt, L. K. Oxenløwe, J. Wang, M. G. Thompson, and A. Laing, "Generation and sampling of quantum states of light in a silicon chip," *Nat. Phys.* **15**, 925–929 (2019).
13. S. Wang, W. Chen, Z.-Q. Yin, H.-W. Li, D.-Y. He, Y.-H. Li, Z. Zhou, X.-T. Song, F.-Y. Li, D. Wang, H. Chen, Y.-G. Han, J.-Z. Huang, J.-F. Guo, P.-L. Hao, M. Li, C.-M. Zhang, D. Liu, W.-Y. Liang, C.-H. Miao, P. Wu, G.-C. Guo, and Z.-F. Han, "Field and long-term demonstration of a wide area quantum key distribution network," *Opt. Express* **22**, 21739–21756 (2014).
14. H.-K. Lo, X. Ma, and K. Chen, "Decoy state quantum key distribution," *Phys. Rev. Lett.* **94**, 230504 (2005).
15. Y.-Y. Ding, H. Chen, S. Wang, D.-Y. He, Z.-Q. Yin, W. Chen, Z. Zhou, G.-C. Guo, and Z.-F. Han, "Polarization variations in installed fibers and their influence on quantum key distribution systems," *Opt. Express* **25**, 27923–27936 (2017).
16. L. Ma, H. Xu, and X. Tang, "Polarization recovery and auto-compensation in quantum key distribution network," *Proc. SPIE* **6305**, 630513 (2006).
17. A. R. Dixon, J. F. Dynes, M. Lucamarini, B. Fröhlich, A. W. Sharpe, A. Plews, S. Tam, Z. L. Yuan, Y. Tanizawa, H. Sato, S. Kawamura, M. Fujiwara, M. Sasaki, and A. J. Shields, "High speed prototype quantum key distribution system and long term field trial," *Opt. Express* **23**, 7583–7592 (2015).
18. Y.-Y. Ding, W. Chen, H. Chen, C. Wang, Y.-P. Li, S. Wang, Z.-Q. Yin, G.-C. Guo, and Z.-F. Han, "Polarization-basis tracking scheme for quantum key distribution using revealed sifted key bits," *Opt. Lett.* **42**, 1023–1026 (2017).
19. H. Zbinden, J. Gautier, N. Gisin, B. Huttner, A. Muller, and W. Tittel, "Interferometry with Faraday mirrors for quantum cryptography," *Electron. Lett.* **33**, 586–588 (1997).
20. S. Wang, W. Chen, Z.-Q. Yin, D.-Y. He, C. Hui, P.-L. Hao, G.-J. Fan-Yuan, C. Wang, L.-J. Zhang, J. Kuang, S.-F. Liu, Z. Zhou, Y.-G. Wang, G.-C. Guo, and Z.-F. Han, "Practical gigahertz quantum key distribution robust against channel disturbance," *Opt. Lett.* **43**, 2030–2033 (2018).
21. N. Gisin, S. Fasel, B. Kraus, H. Zbinden, and G. Ribordy, "Trojan-horse attacks on quantum-key-distribution systems," *Phys. Rev. A* **73**, 022320 (2006).
22. A. Boaron, G. Boso, D. Rusca, C. Vulliez, C. Autebert, M. Caloz, M. Perrenoud, G. Gras, F. Bussi eres, M.-J. Li, D. Nolan, A. Martin, and H. Zbinden, "Secure quantum key distribution over 421 km of optical fiber," *Phys. Rev. Lett.* **121**, 190502 (2018).
23. A. Politi, J. Matthews, M. Thompson, and J. O'Brien, "Integrated quantum photonics," *IEEE J. Sel. Top. Quantum Electron.* **15**, 1673–1684 (2009).
24. S. Bogdanov, M. Y. Shalaginov, A. Boltasseva, and V. M. Shalaev, "Material platforms for integrated quantum photonics," *Opt. Mater. Express* **7**, 111–132 (2017).
25. S. Slussarenko and G. J. Pryde, "Photonic quantum information processing: a concise review," *Appl. Phys. Rev.* **6**, 041303 (2019).
26. Y. Nambu, K. Yoshino, and A. Tomita, "Quantum encoder and decoder for practical quantum key distribution using a planar light-wave circuit," *J. Mod. Opt.* **55**, 1953–1970 (2008).
27. P. Sibson, J. E. Kennard, S. Stanisic, C. Erven, J. L. O'Brien, and M. G. Thompson, "Integrated silicon photonics for high-speed quantum key distribution," *Optica* **4**, 172–177 (2017).
28. D. Bunandar, A. Lentine, C. Lee, H. Cai, C. M. Long, N. Boynton, N. Martinez, C. DeRose, C. Chen, M. Grein, D. Trotter, A. Starbuck, A. Pomerene, S. Hamilton, F. N. C. Wong, R. Camacho, P. Davids, J. Urayama, and D. Englund, "Metropolitan quantum key distribution with silicon photonics," *Phys. Rev. X* **8**, 021009 (2018).
29. Y. Ding, D. Bacco, K. Dalgaard, X. Cai, X. Zhou, K. Rottwitt, and L. K. Oxenløwe, "High-dimensional quantum key distribution based on multicore fiber using silicon photonic integrated circuits," *npj Quantum Inf.* **3**, 25 (2017).
30. H. Semenenko, P. Sibson, A. Hart, M. G. Thompson, J. G. Rarity, and C. Erven, "Chip-based measurement-device-independent quantum key distribution," *Optica* **7**, 238–242 (2020).
31. L. Cao, W. Luo, Y. Wang, J. Zou, R. Yan, H. Cai, Y. Zhang, X. Hu, C. Jiang, W. Fan, X. Zhou, B. Dong, X. Luo, G. Lo, Y. Wang, Z. Xu, S. Sun, X. Wang, Y. Hao, Y. Jin, D. Kwong, L. Kwek, and A. Liu, "Chip-based measurement-device-independent quantum key distribution using integrated silicon photonic systems," *Phys. Rev. Appl.* **14**, 011001 (2020).
32. X. Li, X. Li, M. Ren, J. Zhang, L. Wang, W. Chen, Y. Wang, X. Yin, Y. Wu, Y. Wu, J. An, and J. An, "Interference at the single-photon level based on silica photonics robust against channel disturbance," *Photon. Res.* **9**, 222–228 (2021).
33. I. Lucio-Martinez, P. Chan, X. Mo, S. Hosier, and W. Tittel, "Proof-of-concept of real-world quantum key distribution with quantum frames," *New J. Phys.* **11**, 095001 (2009).
34. W. H. McMaster, "Polarization and the Stokes parameters," *Am. J. Phys.* **22**, 351–362 (1954).
35. Z. L. Yuan, M. Lucamarini, J. F. Dynes, B. Fröhlich, M. B. Ward, and A. J. Shields, "Interference of short optical pulses from independent gain-switched laser diodes for quantum secure communications," *Phys. Rev. Appl.* **2**, 064006 (2014).